The red edge excitation shift phenomenon can be used to unmask protein structural ensembles: implications for NEMO-ubiquitin interactions

*Dragana AM Catici, Hope E Amos, Yi Yang, Jean MH van den Elsen and Christopher R Pudney**

Address. Department of Biology and Biochemistry, Faculty of Science, University of Bath, Bath, BA2 7AY, United Kingdom.

Running title: Unmasking protein conformational plasticity

Abbreviations: NEMO, NF-κB essential modulator; REES, Red edge excitation shift; FEL, Folding energy landscape; Sbi, second immunoglobulin-binding protein ; CSM, center of spectral mass;

Keywords: Red edge excitation shift, free energy landscape, NEMO, protein dynamics, tryptophan fluorescence

Abstract.

To understand complex molecular interactions it is necessary to account for molecular flexibility and the available equilibrium of conformational states. Only a small number of experimental approaches can access such information. Potentially steady-state red edge excitation shift (REES) spectroscopy can act as a qualitative metric of changes to the protein free energy landscape (FEL) and the equilibrium of conformational states. First we validate this hypothesis using a single Trp containing protein, NF-κB essential modulator (NEMO). We provide detailed evidence from chemical denaturation studies, macromolecular crowding studies and the first report of the pressure-dependence of the REES effect. Combined these data demonstrate that the REES effect can report on the 'ruggedness' of the FEL and we present a phenomenological model, based on realistic physical interpretations, for fitting steady-state REES data to allow quantification of this aspect of the REES effect. We test the conceptual framework we have developed by correlating findings from NEMO ligand binding studies with the REES data in a range of NEMO-ligand binary complexes. Our findings shed light on the nature of the interaction between NEMO and poly-ubiquitin, suggesting that NEMO is differentially regulated by poly-ubiqutin chain length and that this regulation occurs via a modulation of the available equilibrium of conformational states, rather than gross structural change. This study therefore demonstrates the potential of REES as a powerful tool for tackling contemporary issues in structural biology and biophysics and elucidates novel information on the structure-function relationship of NEMO and key interaction partners.

Introduction.

There is an increasing realization that the molecular mechanism of many human proteins, particularly those involved in signaling networks, are governed by molecular flexibility and protein structural disorder. That is, proteins that mediate multiple signaling inputs may fold into ligand specific conformations, providing high specificity to a large number of structurally dissimilar ligands [1]. Underpinning these notions is the free energy landscape (FEL) model of protein structure, which interprets molecular heterogeneity (structural disorder and flexibility) as a series of equilibrated energetic minima on a multi-dimensional free energy surface [2]. Proteins that are highly flexible or exist as significantly different discrete conformational states are considered to have a rather 'rugged' FEL. For signaling proteins, understanding how the FEL is altered on ligand binding is key to understanding the molecular mechanism of biological signaling networks.

Detecting ligand induced conformational change (folding) and the relationship to the equilibrium of protein conformational states is challenging. EPR [3] single molecule (SM) [4,5]. Ion mobility mass spectrometry (IM-MS) [6] and NMR [7] studies can be used for this purpose with different levels of resolution. There is now evidence that an optical phenomenon called Red Edge Excitation Shift (REES) may provide unique information on protein conformational change and the equilibrium of conformational states [8]. REES is a phenomenon where low energy excitation of a fluorophore leads to a red shift in the maximum of the emission intensity, $\Delta\lambda_{Em}^{max}$.This phenomenon may manifest where there are a range of discrete fluorophore solvation states and therefore potentially reflects the equilibrium of conformational states that are accessible to a protein [8,9].

The REES effect is governed by interactions between a flourophore and the surrounding solvent in the ground and excited states. REES is observed as a result of the change in the dipole moment of the fluorophore following excitation and the speed at which solvent reorganisation occurs around the newly excited fluorophore [8,9]. In a fully solvated environment, the fluorescence lifetime (τ_F) is much larger than the lifetime of environmental relaxation (τ_S). In this case, the emission wavelength of the chromophore is independent of the excitation wavelength. When $\tau_F < \tau_S$, for example in a rigid molecular environment such as some folded protein states, the intermolecular interactions between the fluorophore and its environment do not change and dipolar relaxation does not occur during fluorescence emission [10,11]. A consequence of this is that the fluorescence emission occurs at higher energy since photons are emitted from the excited state instead of a lower energy relaxed state. It is possible to select for individual solvation environments within an equilibrium by using low energy excitation (photoselection), for example by using lower energy photons or longer wavelengths located at the red edge of the excitation spectrum [12]. Excitation at a lower energy selects for fluorophores in a solvent relaxed environment, which require less energy to become activated. Experimentally one observes a red shift in the emission maximum with respect to excitation wavelength.

There have been a few reports where emission arising from a single Trp residue gives a significant REES effect in the folded and molten globule like states [13], while the REES effect disappears or is rather reduced in unfolded states [14,15]. The REES effect is therefore a unique probe for proteins with a high degree of molecular flexibility resulting in an ensemble of solvent environments around the Trp probe. For proteins, such an ensemble may arise from a broad equilibrium of conformational states, such as in molten globule intermediates of highly flexible or dynamic proteins [14,16,17].

NF-κB essential modulator is the key regulatory element in the NF-κB signaling pathway, controlling much of the nervous and immune system [18]. NEMO regulates the activity of a kinase, IκB kinase-β (IKK-β), which has a diverse range of phosphorylation targets, for example, IκBα [19], huntingtin [20], and insulin receptor 1 (IRS-1) [21]. NEMO putatively ensures the specificity of IKK-β for IκBα, by facilitating the recruitment of IκBα to the kinase [19]. Subsequent proteosomal degradation of IκBα then allows the NF-κB complex to enter the nucleus and induce expression of pro-inflammatory and anti-apoptotic genes. Despite the importance of NEMO to normal human health and disease associated processes, remarkably little is known about the molecular mechanism of action of NEMO and, in particular how NEMO is able to show specificity to a very large number of interaction partners [22]. We have recently provided evidence that NEMO is a flexible protein that undergoes ligand specific conformational change, and have hypothesized that the non-ligand bound protein adopts a broad equilibrium of conformational states [23]. We have previously used the emission of NEMO's single intrinsic Trp residue (W6) as a spectroscopic reporter of ligand-induced NEMO conformational change [23].

Herein we explore the use of REES spectroscopy to inform on the structural and mechanistic determinants of NEMO-ligand binding. First, we develop a new framework for the quantitative interpretation of steady-state REES data, validated by folding and pressure perturbation studies. This then allows us to use the REES data quantitatively for a series of NEMO-ligand bound states. We develop our putative model for the molecular mechanism of NEMO's functional interactions, structure and how this connects to the NEMO free energy landscape and conformational change.

Results and Discussion.

NEMO W6 shows a significant REES signal. Figure 1 shows the variation in emission spectrum (Figure 1A and 1B) and center of spectral mass (CSM) (Figure 1B) of NEMO W6 *versus* excitation wavelength. Typically the magnitude of the steady-state REES phenomenon is reported as the simple difference in CSM or $\Delta\lambda_{Em}^{max}$. From Figure 1, we observe a significant red shift in the emission spectra, with an increase in CSM of 17.7 nm and an increase in $\Delta\lambda_{Em}^{max}$ of 15 nm from λ_{ex} 292-310 nm. Essentially the data are treated by the linear function:

$$CSM = R\lambda_{ex} + CSM_0 \qquad \text{Eq 1.}$$

Where R is the REES magnitude expressed as the change in CSM per nm of the excitation wavelength, λ_{ex}. In this model the y-intercept, CSM_0, does not have an obvious physical meaning and is not typically reported. The solid grey line in Figure 1B *inset* shows the fit of the NEMO REES data to Eq 1, giving $R = 0.96$.

The extracted REES signal with NEMO W6 is large compared to other reported values and is even more significant given that NEMO W6 is already relatively solvent exposed. NEMO W6 is a class III Trp according to the Burstein classification [24]. Class III Trp residues are not typically thought to exhibit a significant REES effect [25] due to the very significant solvent exposure, thus giving rise to an essentially single solvated environment. However, we would point to the example of denatured spectrin which retains a significant REES signature, despite being largely solvent exposed [14]. These findings have been rationalized as reflecting a partially 'unfolded' state with residual structure, comparable to a molten globule state. We have previously suggested that NEMO is a native molten globule [23] and so our findings of a very significant REES effect for an already red-shifted tryptophan are consistent with our previous results. Physically, these findings suggest that NEMO adopts a very broad equilibrium of

conformational states, where there are multiple discrete solvation environments for W6; this could arise both from a series of W6 micro-environments as well as from the stabilization of different Trp rotamers.

Pan *et al* have previously demonstrated that even solvent exposed Trp residues can display a broad range of $\Delta\lambda_{Em}^{max}$ values, arising from different Trp rotamers [26] and calculate a range 344 – 365 nm from molecular dynamics simulations for a range of cyclic peptides. This would seem consistent with our data that show a similar range of $\Delta\lambda_{Em}^{max}$ values, with the largest value being $\Delta\lambda_{Em}^{max}$ = 363 nm at λ_{ex} = 310 nm. This value is the same as for free Trp in our buffer giving $\Delta\lambda_{Em}^{max}$ = 363 nm (Figure 2), suggesting this excitation wavelength is capturing essentially the most red-shifted (solvent exposed) conformational state. Further, Maglia *et al* find a significant REES effect in a single Trp variant of DD-carboxypeptidase attributable to at least three different Trp rotamers [27] . These rotamers may be stabilized through differing H-bonding to the Trp amide carbonyl [28]. As such it is difficult to directly separate the contribution of differing Trp rotamers and larger scale conformational heterogeneity of the peptide backbone to the REES signal. Below, we explore the contribution of different Trp rotamers to the NEMO REES signal in detail.

An artificial REES effect could arise if there is a significant convolution of our Trp signal with the background Tyr signal from NEMO. We excite NEMO from 292 nm upwards specifically so that there is essentially no Tyr emission relative to Trp emission. However, we have explored how a small Tyr signal would affect our REES data by monitoring the REES data for 10 μM Tyr in buffered solution and subtracting this from our NEMO REES data. These data are shown in Figure 2. We find that accounting for the small Tyr signal arising from NEMO's intrinsic Tyr residues gives essentially no difference to our REES data. Further, we have monitored the REES

signal from a single Tyr containing fragment of *Staphylococcus aureus* complement evasion second immunoglobulin-binding protein Sbi domain III and IV that, like NEMO, is composed of a significant fraction of structurally disordered content [29]. These data are shown in Figure 3. We do not find a significant REES signal arising from Tyr emission as is expected because of the symmetrical nature of the Tyr ring system. Together, these data demonstrate that the signal we monitor, as expected, arises essentially entirely from NEMO's single intrinsic Trp.

Establishing a quantitative analysis of REES data. The fit of our REES data to Eq 1 is poor and does not account for the curvature in the data. This is the case for all reported steady-state REES data where a significant number of data point are collected. For REES data to be used in comparative studies, the reporting of *R* in Eq 1 will therefore be wildly inaccurate. To identify a numerical model that would best fit these data we have measured the change in the CSM of NEMO Trp emission across an extended range of Trp absorption (shown in Figure 4), incorporating the emission maximum of the Trp. The REES effect should be observable at the far red edge of the absorption spectrum, with little or no effect at the absorption maximum, since photoselection and hence REES will only occur under low energy excitation. From Figure 4, this trend is apparent. That is, we observe little or no REES effect occurring at the maximum of the excitation spectrum but a significant REES effect at the red edge of the spectrum. We note that the observed changes in CSM are dominated by NEMO's intrinsic Trp residue and not convolved of contributions from Tyr emission since we have shown above that, consistent with theory, Tyr emission does not give a measurable REES effect and does not convolute our REES data (Figure 2). Indeed, we monitor emission from λ_{Ex} = 292 nm, where there is essentially no emission attributable to tyrosine as shown in Figure 2.

We find that the REES data in Figure 4 can be best represented by a Gaussian probability distribution of the form:

$$f(x) = R_0 + \frac{A\sqrt{2/\pi}}{w} exp\left(-2\left(\frac{x-m}{w}\right)^2\right) \qquad \text{Eq 2.}$$

Where A is the area, w is the full width at half-maximal (fwhm), m is the mid-point and R_0 is the y-intercept and $m = \lambda_{REES}^{max}$, where λ_{REES}^{max} is the excitation wavelength that gives the largest change in the emission peak wavelength. The data in Figure 4 are fit to Eq 2 and illustrate the low energy excitation at the red edge of the protein absorption spectrum. The fit of Eq 2 to the experimental data is excellent and captures the expected relationship we describe above.

Potentially, the magnitude of A extracted from fitting Eq 2 to a plot of excitation wavelength *versus* λ_{Em}^{max}, can be used as a qualitative comparator to assess changes in the extent of the REES phenomenon. The magnitude of R_0 should represent the minimum λ_{Em}^{max} value, in the absence of the REES effect. This magnitude is commonly used to reflect the degree of solvent exposure of Trp residues and can be used as a metric of folded/unfolded states. We discuss the interpretation of these values in more detail below. This simple model clearly neglects a range of contributing factors such as the proportion of excited molecules, the small contribution from changing excitation energy at different excitation wavelengths, the number of discrete conformational states that are photo-selectable and the contribution from dipole rotation in the excited electronic state. However, Eq 2, unlike Eq 1 is based on a realistic physical rationale and provides a means to extract meaningful quantitative data from the full range of REES data. We note that other distribution functions can and have been used in relation to extracting information from spectral features, including Lorentz and log-normal distributions [30-31]. Ultimately we do not try and accurately recapitulate the absorbance/excitation spectrum of the fluorophore but instead wish to have a physically meaningful probe beyond the arbitrary use of a simple linear function.

Validating REES as a quantitative probe of molecular heterogeneity. Having established a quantitative model to compare REES data, we now test the hypothesis that REES can be used to reflect changes in the equilibrium of protein conformational states. To achieve this we monitor the REES effect with both denatured and stabilized NEMO as well as pressure-perturbation studies that systematically alter the equilibrium of conformational states and the extracted parameters from fitting the data are given in Table 1.

Typically one does not expect to observe a significant REES effect with denatured protein since the peptide backbone will become fully solvent accessible. In this case the solvent relaxation will be very rapid and no REES effect observed, effectively because there is one discrete solvation state (fully solvated). We have incubated NEMO in 6M guanidine to denature the protein and the corresponding change in the center of spectral mass (CSM) *versus* λ_{ex} is shown in Figure 5. We favor the use of CSM instead of the magnitude of $\Delta\lambda_{Em}^{max}$ as we find this metric gives a more robust REES signal and the magnitude of $\Delta\lambda_{Em}^{max}$ may be highly error prone. However we note the result using $\Delta\lambda_{Em}^{max}$ are essentially the same. A decrease and red-shift in Trp emission is typically grossly correlated with denaturation of proteins. From Figure 5 the incubation with guanidine has significantly denatured NEMO, with a red-shift in CSM giving R_0 = 363.2 ± 0.19 nm to R_0 = 375 ± 0.5 for the native and denatured protein, respectively. Note that this is not the REES effect but reflective of the solvent exposure of NEMO W6 on denaturation. The denatured NEMO shows a dramatically reduced REES effect. Denatured NEMO shows only a 4 nm shift from λ_{ex} 292 to 310 nm and fitting to Eq 1 gives R = 0.22 ± 0.02 and a relative decrease compared to native NEMO of R = 0.23 ± 0.1. Fitting to Eq 2 also gives a large decrease in the REES effect, A = 0.37 ± 0.4. The relative change in the REES effect is similar using either approach and this argues strongly that our fitting approach using Eq 2 is robust.

Macromolecular crowding is a key feature of the intracellular milieu arising from the very high concentrations of other species in the cytosol. Crowding reduces the available solvent for other molecules in solution through the excluded volume effect, which effectively increase the concentration of e.g. protein and restricts the accessible conformational states through hard-core repulsions between the crowding agent and the protein. Macromolecular crowding can alter protein conformation, typically inducing folding and stabilization [32]. Crowding therefore potentially provides a means to explore the contrasting physical effect of denaturation on the REES effect, where the protein is more folded/stabilized. We have used a protein as the crowding agent, Sbi (reported above), instead of a synthetic crowding agent since protein is much more consistent with the intracellular environment. Sbi lacks any intrinsic Trp residues and does not give rise to a REES signal that would convolute our NEMO signal (Figure 3). Incubating NEMO with a high concentration of Sbi (20 mg/ml) gives a dramatic change to the both the absolute Trp emission and also the REES effect as shown in Figure 5. We note that the emission spectra have had the signal arising from Sbi subtracted and so there is no contribution from Sbi Tyr emission. The emission is blue shifted (R_0 = 360.5 ± 0.45 nm) compared to NEMO in the absence of Sbi (R_0 = 363.2 ± 0.19) and more intense (~1.4 times larger emission), suggesting that the NEMO Trp is less solvent exposed and therefore that NEMO is more 'folded' in the crowded environment. Intriguingly the REES effect is much larger in the crowded environment giving a relative increase in *A* of 2.24 ± 0.51. These data therefore suggest that in a crowded environment, more similar to the intracellular milieu, NEMO has a more rugged FEL, able to explore a broader range of conformational states than observed in dilute buffered solution. This is consistent with findings from other studies, for example Dhar *et al* find the phosphoglycerate kinase shows an increase in conformational sampling in a crowded

environment [32]. This is consistent with our putative molecular model of NEMO activity that is based on allosterically regulated NEMO conformational change. Below, we consider the potential mechanistic role of an increased number of available conformational states with respect to ligand interactions.

Based on our native, denatured and stabilized protein analysis (Figure 5) as well as the theoretical basis of the REES effect, the magnitude of REES should be sensitive to changes in the number of discrete equilibrium conformational states. Testing this hypothesis is challenging since few experimental approaches give a direct window into the equilibrium of conformational states. Non-denaturing pressure perturbation is an excellent tool for this purpose since it acts to perturb a pre-existing equilibrium of structural states characterized by different energy minima on the protein FEL [33] and has been used for this purpose in a number of studies [34-36]. Crucially pressure, unlike temperature, does not alter the internal energy of the system, which might otherwise be a confounding factor for REES measurements. The observation of a significant pressure dependence on the REES effect itself would therefore be powerful evidence that REES is sensitive to the equilibrium of protein conformational states.

We have previously found that increasing pressure causes a decrease in W6 emission, suggesting increased solvent exposure [23]. This finding is corroborated by a red shift in the W6 CSM with increasing pressure (Figure 6A), giving an increase of 3.0 nm at λ_{ex} = 292 nm. We note that the CSM value is rather larger than reported for the denaturation study above (Figure 5A and 5B) and this is due to a different spectral window used to calculate the CSM for the pressure studies. This was necessary due to the optical setup of the pressure cell. The $\Delta\lambda_{Em}^{max}$ value of W6 at 1 bar is similar to that reported above, giving $\Delta\lambda_{Em}^{max}$ = 348 nm at 10 °C, 1 bar and λ_{ex} = 295 nm. Increasing pressure leads to a large CSM at higher λ_{ex} values, giving an increase of

8.9 nm at λ_{ex} = 310 nm from 1 to 2000 bar. These data suggest that the REES effect itself is pressure-dependent. We note that we do not observe any REES effect with free Trp in buffered solution at any pressure (Figure 6B) and the changes we observe are protein specific. Fitting the REES data to Eq 4 gives the pressure dependence of *A,* shown in Figure 6C as the change in the fraction of *A* across the pressure range. The pressure dependence data can be adequately fit to a simple, phenomenological model that implies a single transition between two states with changing hydrostatic pressure as used previously [23]:

$$\frac{A_i}{\sum A}(p,T) = \frac{K(p,T)}{1+K(p,T)} = \frac{\exp(lnK_0 - \Delta V_A p/R_p T)}{1+\exp(lnK_0 - \Delta V_A p/R_p T)} \qquad \text{Eq 3.}$$

Where R_p = 83.13 cm3 mol^{-1} bar K^{-1} when the pressure, *p*, is measured in bar, K_0 is the equilibrium constant for the change in the relative population of the *i*th conformational state represented by the magnitude of *A* from Eq 4, extrapolated to 0 bar and ΔV_A is the apparent difference in the volume associated with this equilibrium transition.

Fitting the data in figure 6 to Eq 3 gives a negative activation volume ΔV = -24.7 ± 4.7 cm^3 mol^{-1}. We have previously measured ΔV for W6 emission and find (as we show here) that the emission decreases across the pressure range giving ΔV = 0.81 ± 0.03 cm^3 mol^{-1} [23]. The difference in sign is simply attributable to relative change in direction of the specific signal. What is important is that the magnitude of ΔV is much larger for the REES effect compared to W6 emission. Indeed, this magnitude of pressure dependence is more consistent with global metrics of NEMO conformational change previously measured using the pressure dependence of 8-anilino naphthalene sulfonate (ANS) emission [23]. |The REES signal may therefore be reflective of the broader equilibrium of NEMO conformational states at sites distal to W6. That is, these two values are not necessarily comparable, reflecting different aspects of the W6 molecular environment. The key finding from the pressure data in the present context is that the

REES effect itself is pressure-dependent with the magnitude of *A* increasing with pressure. Given that pressure acts to perturb the equilibrium of conformational states, this observation suggests that the magnitude of *A* extracted from Eq 2 is exquisitely sensitive to this equilibrium.

Our findings from denaturation, pressure and macromolecular crowding measurements suggest that the REES effect as monitored by Eq 2, is sensitive to changes in the equilibrium of conformational states, e.g. by unfolding (chemical denaturation), stabilization/folding (macromolecular crowding) or direct perturbation (pressure). As such, we suggest that the magnitude of the REES effect can be used as a proxy for the protein free energy landscape (FEL), reflecting the distribution of discrete conformational sub-states. Based on our observations we have developed a conceptual framework for interpreting protein REES data using Eq 2, shown in Figure 7. Our interpretation of the present data moves beyond current applications by explicitly recognizing the information content that arises from the curvature of the REES data. Within this framework, the changing curvature of the REES data, reflected by the magnitude of *A* from Eq 2, describes the progression to a larger or smaller number of discrete conformational states, a rugged or flat FEL, respectively. In addition the intercept with the y-axis, R_0, describes whether the protein tends towards a folded or unfolded state, in exactly the same way as per the normal analysis of Trp emission in protein folding studies, but with the added benefit that it takes account of cases where the peak maximum of the emission band shifts with excitation wavelength. It is important to note that the terms folded and unfolded encompass more minor conformational changes also. So for highly flexible and dynamic proteins a blue shifted CSM may simply reflect a more compact conformational state (as we suggest is the case from the crowding experiment shown in Figure 5), without requiring a large scale folding event.

It is important to recognize that REES data from protein Trp residues will be convolved of the signal arising from different Trp rotamers [26]. However, our observations suggest that at least for NEMO, the REES signal is not *significantly* convolved of a signal from Trp rotamers. That is, the pressure dependence of the REES gives a very large activation volume (-24.7 ± 4.7 cm^3 mol^{-1}), much larger than based on Trp emission alone (-1.6 ± 0.4 cm^3 mol^{-1}) and more consistent with measurements that reflect global NEMO conformational change [23]. Moreover, we demonstrate below that ligand binding at sites that are not located near the Trp residue significantly alter the REES signal and this is powerful evidence that the NEMO REES signal is dominated by the proteins global structural ensemble.

Novel insight from REES on the nature of NEMO allostery and ligand induced conformational change. Having established that the REES effect, specifically the use of Eq 2, can be used as a proxy for the protein free energy landscape, we now consider how the NEMO REES signal varies upon ligand binding. These data should give more direct insight into the mechanism of ligand induced conformational change and the relationship to the protein FEL. The REES data for NEMO ligand bound states are shown in Figure 8A and 8B with the solid lines representing the fit to Eq 2. The resulting extracted values of *A* from Eq 2 are given in Table 1 and also as an inset bar chart in Figure 8. For clarity, we report the *relative* change in *R* and *A* compared to NEMO alone, extracted from Eq 1 and 2, respectively.

Figure 8A shows NEMO alone and bound to either a peptide mimic of IκBα or IKK-β. The IKKβ peptide (termed the NEMO binding domain, NBD) contains two Trp residues and so is not suitable for the present study as the signal from the peptide would confound our analysis of the single NEMO Trp. Instead we have replaced these Trp residues with a conservative amino acid, Phe, and we call this peptide NBD-Phe. We find that this modified peptide binds to NEMO,

giving a decrease in W6 emission of ~ 50 %. From Table 1 and Figure 8A there is a significant difference in the magnitude of *A* depending on the ligand bound form of NEMO. That is, *A* decreases significantly on IκBα peptide binding ($A = 0.85 \pm 0.04$) but increases significantly on NBD-Phe binding ($A = 1.33 \pm 0.3$). If we fit the ligand binding data shown in Figure 8A to the simple linear function described by Eq 1 we find a different trend. That is, from Eq 3, IκBα peptide binding increases the relative magnitude of the REES effect ($R = 1.35 \pm 0.1$) and IKK-β peptide binding gives essentially no change in the relative magnitude of the REES effect ($R = 0.98 \pm 0.1$). From Figure 8A it is apparent that the REES data are not equivalent with NEMO bound to NBD-Phe and NEMO alone as suggested by the fit to Eq 1. Instead the major difference is in the curvature of the data and this is captured by the use of Eq 2. Based on our findings from the pressure data discussed above, we suggest that these data reflect a decrease in the number of discrete conformational states on IκBα binding, but an increase in the number of discrete conformational states on IKK-β binding. This oppositional relationship is supported by our previous NEMO-ligand binding studies monitoring the change in ANS emission [23], which suggest the exposure of hydrophobic residues on IKK binding and the burying of hydrophobic residues on IκBα.

NEMO comprises a specific domain that non-covalently binds poly-ubiquitin. We have previously found that binding of long chain-length 'free' M1-linked poly-ubiquitin chains to NEMO allosterically regulates ligand affinity and potentially cellular localization based on evidence from stopped-flow and liposome binding assays [23]. Poly-ubiquitin is found as a range of chain-lengths in the cell and we have previously provided evidence from ANS binding studies that NEMO undergoes different conformational change depending on the chain-length of non-covalently bound poly-ubiquitin [23]. We have explored the REES effect on NEMO W6 in the

presence of both short (4-mer; Ub_4) and long (10-mer; Ub_{10}) poly-ubiquitin chains, shown in Figure 8B. From the resulting values of *A*, given in Table 1, Ub_4 binding gives a decrease in *A* (*A* = 0.77 ± 0.05), but Ub_{10} gives an increase (*A* = 1.23 ± 0.1). A simple linear fit to Eq 1 suggests no difference in REES with either chain length giving *A* of ~ 1 within error (Table 1), despite obvious differences in the curvature of the data sets. The absolute magnitude of the REES difference is small and we would focus on the broad trend we observe that potentially suggests that longer chain lengths induce a broader range of accessible NEMO conformational states.

Based on the most current NEMO structural model the poly-ubiquitin binding site is not located near the native Trp residue [23,37]. That we observe a significant change in the REES effect for this Trp is consistent with the notion that poly-ubiquitin binding alters NEMO conformation or dynamics in an allosteric fashion. The trend for a decrease in REES with shorter poly-ubiquitin chain lengths and an increase at longer chain-lengths mirrors the binding of ANS that we have reported previously [23]. That is, we observe a decrease in ANS emission (suggesting burying of hydrophobic residues) at short chain lengths and an increase (suggesting exposure of hydrophobic residues) at longer chain lengths. Combined, these data suggest that shorter poly-ubiquitin chain lengths may drive compaction (burying of hydrophobics and a reduction in the equilibrium of conformational states) and longer chain lengths may drive expansion (exposure of hydrophobics and an increased equilibrium of conformational states) of NEMO. Our REES data further suggest that these changes are not large scale folding or unfolding events since the R_0 values (Table 1) are essentially the same. Based on these data we hypothesise that the allosteric regulation of NEMO by poly-ubiquitin occurs by modulating the available equilibrium of conformational states, rather than gross structural change.

Mechanistic consequences for the NEMO-ubiquitin interaction. There is a great deal of contemporary interest in the relationship between the equilibrium of native protein conformational states and how this equilibrium changes upon ligand binding [38-41]. Based on insight from our current data, we suggest that NEMO predominately utilizes a conformational selection model of ligand binding and we show this as a schematic in Figure 9. That is, NEMO adopts a range of equilibrated conformational states represented by discrete energetic minima on the protein FEL. Ligand binding occurs at one of these pre-existing conformers, shifting the equilibrium towards the ligand bound population. For example, as we show above, IκBα binding gives a significant reduction in the number of NEMO conformers, implying a less rugged FEL for the binary complex. However, we would extend this model to suggest that ligand binding may also induce new conformational states, as well as expanding the number of discrete states within the population (a more rugged FEL) as with NBD and Ub_{10}. A potential mechanistic rationale for this finding is that the new conformational space allows new molecular interactions, not accessible to the non-ligand bound protein alone. Indeed, we have previously found that Ub_{10} enhances the affinity of NEMO for IKK-β and IκBα and promotes liposome association [23]. Based on our present data we would hypothesise that this allosteric effect is achieved by exposing new high affinity binding sites or additional binding determinants for these species.

A recent study by Bagnéris *et al* [37] have modeled the NEMO structure as a parallel coiled coil and have provided experimental evidence for this structural model from PELDOR (pulsed electron electron double resonance studies). We have previously found from far-UV CD studies that NEMO is composed primarily of α-helical (~50 %) and random coil (~40%) and our present data suggest that the NEMO structure occupies an equilibrium of conformational states. We suggest that these data can be resolved by a model where NEMO is in a dynamic equilibrium

between well folded (coiled coil) and locally unfolded (random coil) states (the dotted connecting lines in Figure 9). This dynamic equilibrium can then be differently stabilized on ligand binding, with IκBα giving rise to an increased proportion of folded content and IKK-β/poly-ubiquitin giving more unstructured content. This model would then be consistent with the PELDOR data, our previous ANS binding studies and the present REES data.

Methods

Protein expression and purification. Full length human NEMO was expressed and purified essentially as described previously [23]. Purified protein was dialysed extensively into a buffer comprising 50 mM Tris-Cl pH 8.0, 50 mM NaCl and 5 mM DTT. All measurements were made in this buffer unless otherwise stated. IKK-β and IκBα peptides were commercially synthesised by Genscript, having a purity of > 98 % and are of the sequence TALDFSFLQTE and DDRHDSGLDSMKD, respectively. The IKK-β peptide was modified such that the two native Trp residues were replaced with Phe residues. M1-linked poly-ubiquitin was purchased from Viva Bioscience. *Staphylococcus aureus* immune modulator protein fragment Sbi-III-IV K173A was expressed and purified essentially as described previously [44]. Protein concentration used was between 1 and 5 μM. Peptide concentrations were 1 mM and poly-ubiquitin concentrations were 1 μM.

Red edge excitation and high-pressure measurements. All fluorescence measurements were performed using a Perkin Elmer LS50B Luminescence Spectrometer (Perkin Elmer, Waltham, MA, USA) connected to a circulating water bath for temperature regulation (± 1 °C). Samples were incubated for 5 minutes at the given conditions prior to recording measurements. Measurements were performed at 10°C, unless otherwise stated. Excitation and emission slit widths were 5 nm except for pressure experiments where they were 10 nm. The larger slit width was required due to the optical setup of the pressure cell to ensure a low signal-to-noise for the W6 emission signal. For NEMO red edge excitation scans, tryptophan emission was monitored from 315 to 550 nm. The excitation wavelength was subsequently increased in 1nm steps for a total of 19 scans. For Sbi-III-IV, red edge excitation scans, tyrosine emission was monitored from 294 to 400 nm, with the excitation wavelength set at 274 nm. Similarly, the excitation

wavelength was subsequently increased in 1nm steps for a total of 19 scans. The corresponding buffer or buffer and ligand control was subtracted from the spectra for each experimental condition. Specifically, we note that for the crowding experiment with Sbi, we subtract the emission from the Sbi so our signal is not convolved of Sbi Tyr emission in any way.

An ISS high-pressure cell (ISS, Champaign, UL, USA), fitted with a custom fiber optic mounting to the fluorimeter and connected to a circulating water bath for temperature regulation was used to record all high-pressure measurements. For NEMO high-pressure red edge excitation measurements, tryptophan emission was monitored between 325-450 nm.

The center of spectral mass (CSM) was calculated using the following equation:

$$CSM = \frac{\sum(f_i x\, \lambda_{Em})}{\sum(f_i)} \qquad \text{Eq 4}$$

Where f_i is the measured fluorescence intensity and λ_{em} is the emission wavelength. We would stress the importance of using a consistent wavelength range when reporting CSM data, as the magnitude will be dependent on the wavelength range chosen. As such we report the CSM across the emission range 325 – 450 nm or 335 – 450 nm for pressure experiments.

Author Contributions

D.A.M.C, H.E.A, Y.Y and C.R.P performed experiments. D.A.M.C, J.M.H.E and C.R.P wrote the main manuscript text. D.A.M.C and C.R.P prepared the figures. All authors reviewed the manuscript.

Acknowledgements

We are grateful to Dr Ventsi Valev and Professor Joseph Lakowicz for helpful input and discussions. This work was funded by the UK Royal Society, the UK Biochemical Society, the University of Bath and the Engineering and Physical Sciences Research Council (EPSRC) fund DAMC's studentship.

References

1. Uversky VN (2013) A decade and a half of protein intrinsic disorder: Biology still waits for physics. *Protein Sci.* **22,** 693–724.
2. Tsai CJ, Buyong M, Sham YY, Kumar S & Nussinov R (2001) Structured disorder and conformational selection. *Proteins Struct. Funct. Genet.* **44,** 418–427.
3. Sobolewska-Stawiarz A, Leferink NG, Fisher K, Heyes DJ, Hay S, Rigby SE & Scrutton NS (2014) Energy landscapes and catalysis in nitric-oxide synthase. *J. Biol. Chem.* **289,** 11725–11738.
4. Laursen T, Singha A, Rantzau N, Tutkus M, Borch J, Hedegård P, Stamou D, Møller BL & Hatzakis NS (2014) Single molecule activity measurements of cytochrome P450 oxidoreductase reveal the existence of two discrete functional states. *ACS Chem. Biol.* **9,** 630–634.
5. Ferreon AC M, Ferreon JC, Wright PE & Deniz A (2013) Modulation of allostery by protein intrinsic disorder. *Nature* **498,** 390–394 .
6. Ruotolo BT, Giles K, Campuzano I, Sandercock AM, Bateman RH & Robinson CV (2005) Evidence for macromolecular protein rings in the absence of bulk water. *Science.* **310**, 1658-61.
7. Sugase K, Dyson HJ, Wright PE (2007) Mechanism of coupled folding and binding of an intrinsically disordered protein. *Nature* **447,** 1021–1025 .
8. Chattopadhyay A & Haldar S (2014) Dynamic insight into protein structure utilizing red edge excitation shift. *Acc. Chem. Res.* **47,** 12–19 .
9. Demchenko A P, (2002) The red-edge effects: 30 years of exploration. *Luminescence* **17,** 19–42 .
10. Weber G & Shinitzky M (1970) Failure of Energy Transfer between Identical Aromatic Molecules on Excitation at the Long Wave Edge of the Absorption Spectrum. *Proc. Natl. Acad. Sci. U. S. A.* **65,** 823–830 .
11. Galley WC & Purkey RM (1970) Role of heterogeneity of the solvation site in electronic spectra in solution. *Proc. Natl. Acad. Sci. U. S. A.* **67,** 1116–1121.
12. Chattopadhyay A & Mukherjee S (1999) Red Edge Excitation Shift of a Deeply Embedded Membrane Probe: Implications in Water Penetration in the Bilayer. *J. Phys. Chem. B* **103,** 8180–8185 .
13. Kelkar D, Chaudhuri A, Haldar S & Chattopadhyay A (2010) Exploring tryptophan dynamics in acid-induced molten globule state of bovine alpha-lactalbumin: a wavelength-selective fluorescence approach. *Eur. Biophys. J.* **39,** 1453–1463 .
14. Mitra M, Chaudhuri A & Patra M (2015) Organization and Dynamics of Tryptophan Residues in Brain Spectrin : Novel Insight into Conformational Flexibility. J Fluoresc. **25**, 707-17 .
15. Chattopadhyay A, Rawat SS, Kelkar D, Ray S & Chakrabarti A (2003) Organization and dynamics of tryptophan residues in erythroid spectrin: novel structural features of

denatured spectrin revealed by the wavelength-selective fluorescence approach. *Protein Sci.* **12,** 2389–2403.

16. Jain N, Bhasne K, Hemaswasthi M & Mukhopadhyay S (2013 Structural and dynamical insights into the membrane-bound α-synuclein. *PLoS One* **8,** e83752.

17. Rawat S S, Kelkar D & Chattopadhyay A (2004) Monitoring gramicidin conformations in membranes: a fluorescence approach. *Biophys. J.* **87,** 831–843 .

18. Gilmore T D (2006) Introduction to NF-kappaB: players, pathways, perspectives. *Oncogene* **25,** 6680–6684.

19. Schröfelbauer B, Polley S, Behar M, Ghosh G & Hoffmann A (2012) NEMO Ensures Signaling Specificity of the Pleiotropic IKKβ by Directing Its Kinase Activity toward IκBα. *Mol. Cell* **47,** 111–121 .

20. Thompson, L. M. Aiken CT, Kaltenbach LS, Agrawal N, Illes K, Khoshnan A, Martinez-Vincente M, Arrasate M, O'Rourke JG, Khashwji H, Lukacsovich T, Zhu YZ, Lau AL, Massey A, Hayden MR, Zeitlin SO, Finkbeiner S, Green KN, LaFerla FM, Bates G, Huang L, Patterson PH, Lo DC, Cuervo AM, Marsh JL & Steffan JS (2009) IKK phosphorylates Huntingtin and targets it for degradation by the proteasome and lysosome. *J. Cell Biol.* **187,** 1083–1099 .

21. Nakamori Y, Emoto M, Fukuda N, Taguchi A, Okuya S, Tajiri M, Miyagishi M, Taira K, Wada Y & Tanizawa Y (2006) Myosin motor Myo1c and its receptor NEMO/IKK-γ promote TNF-α-induced serine307 phosphorylation of IRS-1. *J. Cell Biol.* **173,** 665–671.

22. Fenner B J, Scannell M & Prehn JHM (2010) Expanding the substantial interactome of NEMO using protein microarrays. *PLoS One* **5,** e8799.

23. Catici DAM, Horne J E, Cooper GE & Pudney CR (2015) Poly-ubiquitin drives the molecular interactions of NF-κB essential modulator by allosteric regulation. *J. Biol. Chem.* **290**, 14130-9.

24. Reshetnyak YK, Koshevnik Y & Burstein EA (2001) Decomposition of Protein Tryptophan Fluorescence Spectra into Log- Normal Components . III . Correlation between Fluorescence and Microenvironment Parameters of Individual Tryptophan Residues. **81,** 1735-58.

25. Demchenko AP (1988) Red-edge-excitation fluorescence spectroscopy of single-tryptophan proteins. *Eur. Biophys. J.* **16,** 121–129.

26. Pan CP, Callis P R & Barkley MD (2006) Dependence of tryptophan emission wavelength on conformation in cyclic hexapeptides. *J. Phys. Chem. B* **110,** 7009–7016 .

27. Maglia G, Jonckheer A, De Maeyer M, Frère J-M & Engelborghs Y (2008) An unusual red-edge excitation and time-dependent Stokes shift in the single tryptophan mutant protein DD-carboxypeptidase from Streptomyces: the role of dynamics and tryptophan rotamers. *Protein Sci.* **17,** 352–361 .

28. Xu J, Chen J, Toptygin D, Tcherkasskaya O, Callis P, King J, Brand L & Knutson JR (2009) Femtosecond fluorescence spectra of tryptophan in human gamma-c rystallin mutants: Site-dependent ultrafast quenching. *J. Am. Chem. Soc.* **131,** 16751–16757 .

29. Upadhyay A, Burman JD, Clark EA, Leung E, Isenman DE, van den Elsen JM & Bagby S (2008) Structure-function analysis of the C3 binding region of Staphylococcus aureus immune subversion protein Sbi. *J. Biol. Chem.* **283,** 22113–22120.
30. Djikanović D, Kalauzi A, Jeremić M, Mićić M & Radotić K. (2007) Deconvolution of fluorescence spectra: Contribution to the structural analysis of complex molecules. *Colloids Surfaces B Biointerfaces* **54,** 188–192.
31. Caarls W, Soledad Celej M, Demchenko AP & Jovin TM. (2010) Characterization of coupled ground state and excited state equilibria by fluorescence spectral deconvolution. *J. Fluoresc.* **20,** 181–190.
32. Dhar A, Samiotakis A, Ebbinghaus S, Nienhaus L, Homouz D, Gruebele M & Cheung MS (2010) Structure, function, and folding of phosphoglycerate kinase are strongly perturbed by macromolecular crowding. *Proc Natl Acad Sci U S A.* **107**,17586-91.
33. Akasaka K (2006) Probing conformational fluctuation of proteins by pressure perturbation. *Chem. Rev.* **106,** 1814–1835 .
34 Pudney CR, Hay S, Levy C, Pang J, Sutcliffe MJ, Leys D & Scrutton NS (2009)Evidence to support the hypothesis that promoting vibrations enhance the rate of an enzyme catalyzed H-tunneling reaction. *J. Am. Chem. Soc.* **131,** 17072–17073 .
35. Hay S, Pudney CR, Sutcliffe MJ & Scrutton NS (2010) Probing active site geometry using high pressure and secondary isotope effects in an enzyme-catalysed 'deep' H-tunnelling reaction. *J. Phys. Org. Chem.* **23,** 696–701 .
36. Collins M D, Kim CU & Gruner SM (2011) High-pressure protein crystallography and NMR to explore protein conformations. *Annu. Rev. Biophys.* **40,** 81–98.
37. Bagnéris C, Rogala KB, Baratchian M, Zamfir V, Kunze MB, Dagless S, Pirker KF, Collins MK, Hall BA, Barrett TE & Kay CW (2015) Probing the Solution Structure of IκB Kinase (IKK) Subunit γ and its Interaction with Kaposi′s Sarcoma Associated Herpes Virus Flice Interacting Protein and IKK Subunit β by EPR Spectroscopy. *J. Biol. Chem.* **290**, 16539-49
38. Vogt AD & Di Cera E (2013) Conformational selection is a dominant mechanism of ligand binding. *Biochemistry* **52,** 5723–5729.
39. Okazaki K-I & Takada S (2008) Dynamic energy landscape view of coupled binding and protein conformational change: induced-fit versus population-shift mechanisms. *Proc. Natl. Acad. Sci. U. S. A.* **105,** 11182–11187.
40. Wlodarski T & Zagrovic B (2009) Conformational selection and induced fit mechanism underlie specificity in noncovalent interactions with ubiquitin. *Proc. Natl. Acad. Sci. U. S. A.* **106,** 19346–19351 .
41. Nussinov R, Ma B & Tsai CJ (2014) Multiple conformational selection and induced fit events take place in allosteric propagation. *Biophys. Chem.* **186,** 22–30 .

Tables

Table 1. Results of fitting NEMO-ligand complex REES data to Eq 1 and Eq 2.

	A^a	R_0 (nm)	R^a
Native, denatured, crowded			
$NEMO_{native}$	1 ± 0.1	363.2 ± 0.19	1 ± 0.13
$NEMO_{denat}$	0.37 ± 0.4	375.0 ± 0.5	0.21 ± 0.01
NEMO + Sbi (20 mg/ml)	2.24 ± 0.51	360.5 ± 0.45	1.07 ± 0.12
Binding partners			
NEMO + IκBα	0.85 ± 0.04	364.1 ± 0.62	1.35 ± 0.1
NEMO + NBD-Phe	1.33 ± 0.31	363.0 ± 1.5	0.98 ± 0.1
NEMO + Ub_4	0.77 ± 0.05	364.6 ± 0.77	1.06 ± 0.1
NEMO + Ub_{10}	1.23 ± 0.0.1	362.8 ± 0.25	0.93 ± 0.11

a, Values are relative to the extracted value for NEMO alone.

Figure legends

Figure 1. NEMO W6 displays a significant REES effect. **A**, Contour plot showing the change in the structure of the emissions spectra with increasing λ_{Ex}. The dashed white line shows the change in the λ_{Em}^{max} for each emission spectrum and is to aid the eye only. **B,** Relative change the intensity of W6 emission (λ_{Em}^{max} shown as a dashed red line to aid the eye) for increasing λ_{Ex}. *Inset*, the corresponding change in CSM with λ_{Ex} calculated from Eq 1. Solid line is the fit to Eq 1.

Figure 2. **A,** Emission spectrum of tyrosine excited at 292 nm. The raw spectra, buffer spectra and difference spectrum are shown. **B,** The emission spectrum of 2 μM NEMO and 10 μM tyrosine (from **A**) excited at 292 nm. The total emission of Tyr is 0.5 % of the total NEMO emission. **C,** The emission spectrum of NEMO excited at 292 nm (black line; left axis) and 310 nm (blue line; right axis). The grey and cyan lines show the subtraction of the emission spectrum of 10 μM Tyr from the NEMO emission spectra at 292 nm and 310 nm, respectively. The red dashed line shows the emission spectrum of L-Trp (excitation at 310 nm) in the same buffer, with the intensity normalized for comparison. **D,** The resulting REES effect for NEMO (black) and for the Tyr subtracted spectra for 10 μM Tyr (red).

Figure 3. Sbi does not display a significant REES effect. **A**, Contour plot showing the change in the structure of the emissions spectra with increasing λ_{Ex}. The dashed white line shows the change in the λ_{Em}^{max} for each emission spectrum to aid the eye only. **B,** Relative change the intensity of W6 emission (λ_{Em}^{max} shown as a dashed black lineto aid the eye for increasing λ_{Ex}. *Inset,* the corresponding change in CSM with λ_{Ex} calculated from Eq 1. Solid line is the fit to Eq 3.**Figure 4.** A phenomonological model to fit REES data. The excitation spectrum of NEMO W6 (emission

at 348 nm) is shown as a grey line (right-hand axis) across an extended wavelength range. The variation in CSM with λ_{Ex} for NEMO W6 is shown as black circles (lef-hand axis) and the solid line is the fit to Eq 2 but with a sum of two Gaussians to capture the ascending and descending limb of the REES data.

Figure 5. The effect of denaturation and crowding on NEMO REES. The REES data for native NEMO (black circles), denatured NEMO (red circles) and crowded (20mg/ml Sbi) NEMO are fit to Eq 2 (solid lines). The inset shows the extracted value of *A* from Eq 4. The error bars are the standard deviation from 3 measurements.

Figure 6. The REES effect is sensitive to pressure variation. **A,** Variation in REES with increasing pressure. Dashed lines are the fits to Eq 4. **B,** Comparison of low and high pressure REES data for NEMO W6 and free Trp. The data show the difference in CSM (ΔCSM) *versus* pressure. **C,** The pressure dependence of *A* extracted from the fits in panel A. The dashed line is the fit to Eq 3.

Figure 7 Conceptual framework for the interpretation of tryptophan REES data in proteins.

Figure 8. Ligand induced conformational change occurs by altering the existing equilibrium of NEMO conformational states. **A,** Change in REES on binding IκBα and IKK-β peptides. Solid line is the fit to Eq 2. *Inset* the extracted relative magnitude of *A* from the fit. **B,** Change in REES on binding different poly-ubiquitin chain lengths. Solid line is the fit to Eq 2. *Inset* the extracted relative magnitude of *A* from the fit. The error bars are the standard deviation from 3 measurements.

Figure 9. A schematic depiction of the putative change in NEMO's free energy landscape on interaction with IKK-β, IκBα and different chain-lengths of poly-ubiquitin. The black energy energy (E) barrier (left) represent the small number of discrete conformational states, tending

towards a single major conformational state (orange circle) and the right hand barrier represent an increased range of discrete conformational states (coloured circles). We suggest ligand binding modulates the available equilibrium of conformational states and that this acts as part of the molecular control of NEMO's functional interactions. The putative NEMO structure is shown as coloured ribbons (solved NEMO structures deposited in the PDB; 3BRV, 3CL3, 2ZVN and 2JVX; adapted from ref 23), connected by regions (dotted lines) which can change conformational state depending on the nature of the specific NEMO-ligand complex

Figures

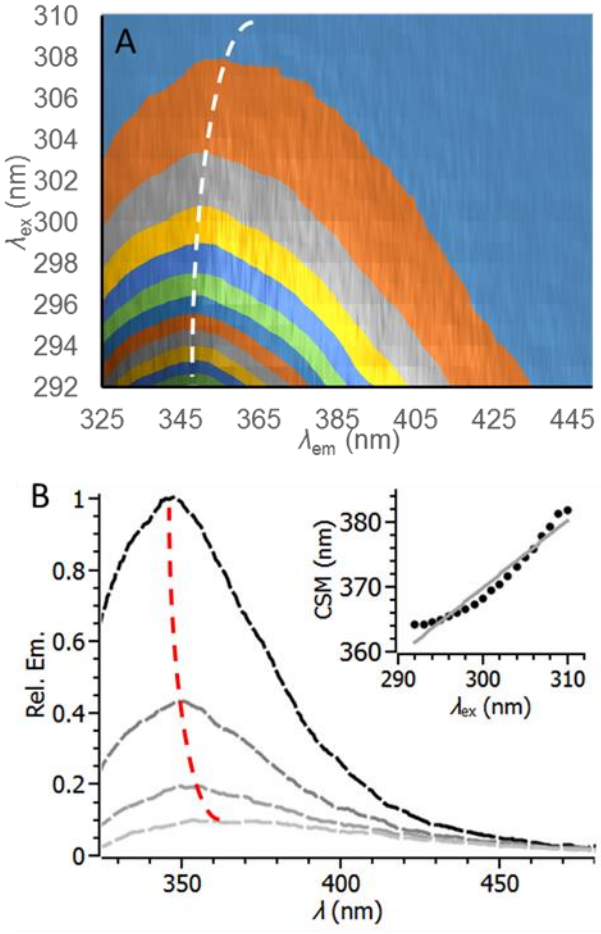

Figure 1.

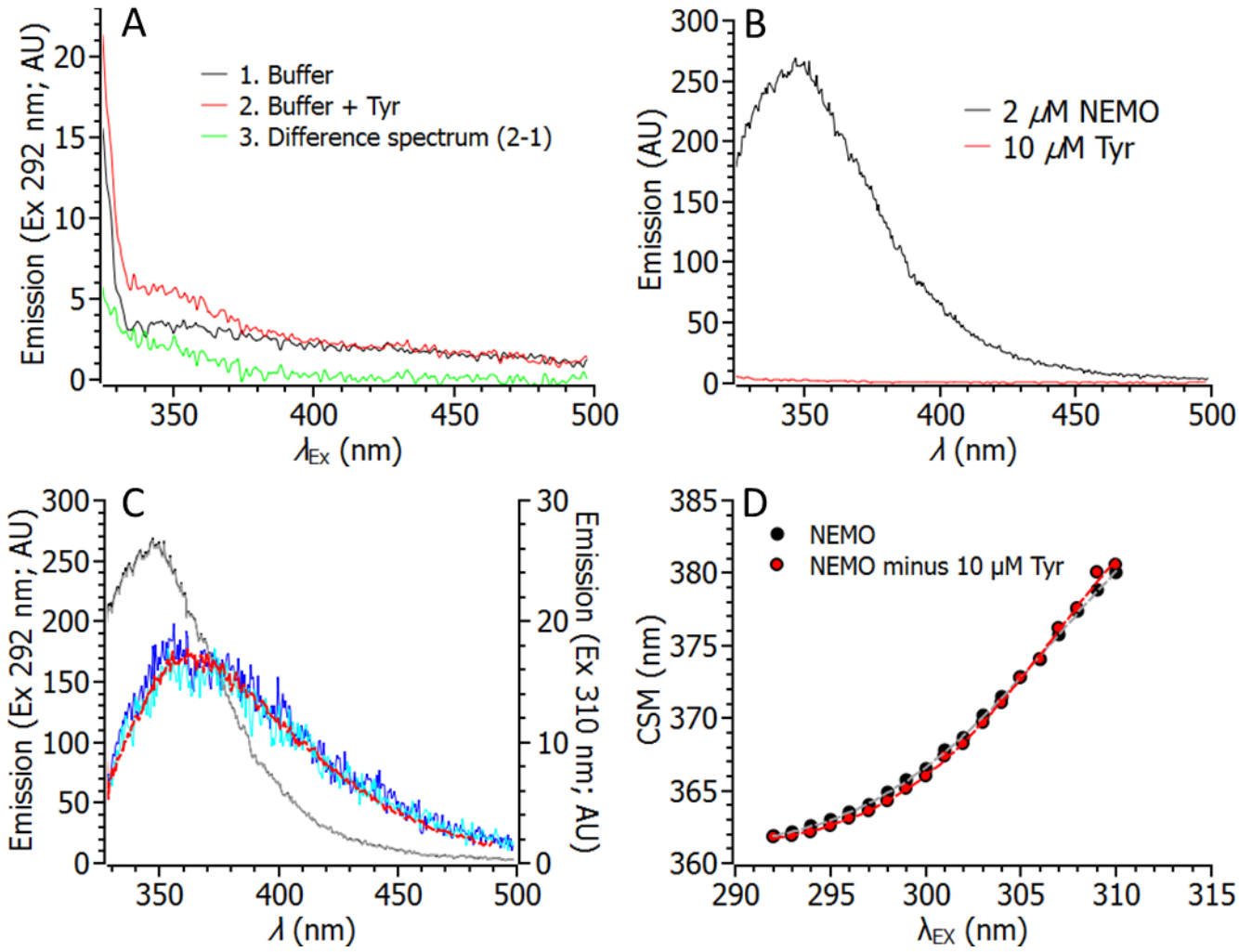
A
1. Buffer
2. Buffer + Tyr
3. Difference spectrum (2-1)
Emission (Ex 292 nm; AU)
λEx (nm)
B
2 μM NEMO
10 μM Tyr
Emission (AU)
λ (nm)
C
Emission (Ex 292 nm; AU)
Emission (Ex 310 nm; AU)
λ (nm)
D
NEMO
NEMO minus 10 μM Tyr
CSM (nm)
λEX (nm)

Figure 2.

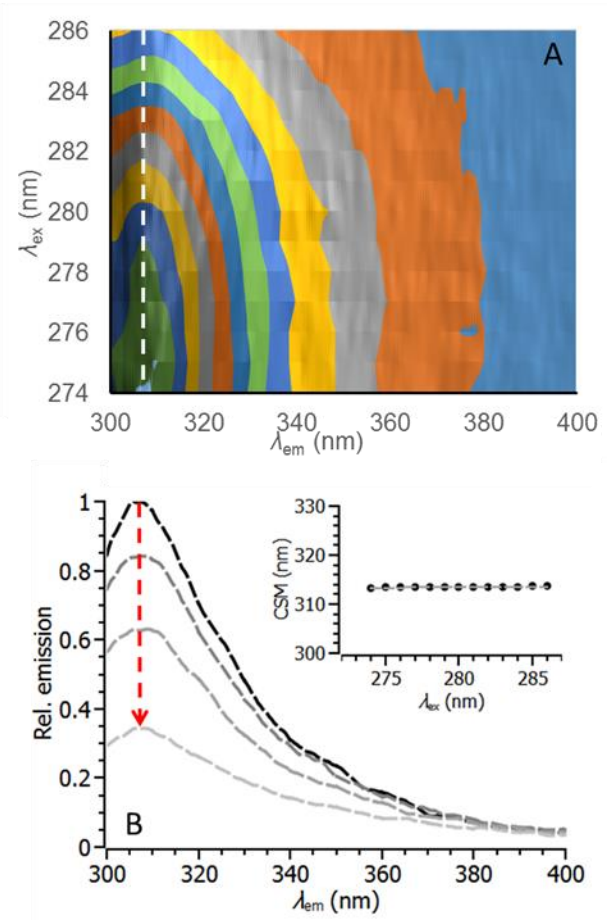
A
286
284
282
280
278
276
274
λ_{ex} (nm)
300
320
340
360
380
400
λ_{em} (nm)
B
1
0.8
0.6
0.4
0.2
0
Rel. emission
330
320
310
300
CSM (nm)
275
280
285
λ_{ex} (nm)

Figure 3.

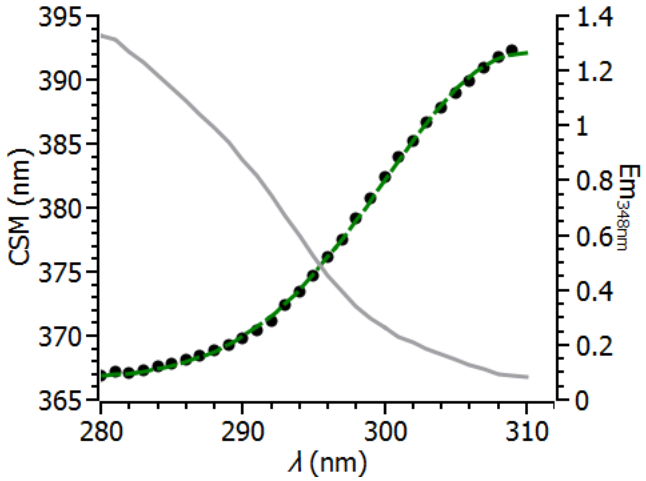
395
390
385
380
375
370
365
CSM (nm)
280
290
300
310
λ (nm)
1.4
1.2
1
0.8
0.6
0.4
0.2
0
Em348nm

Figure 4.

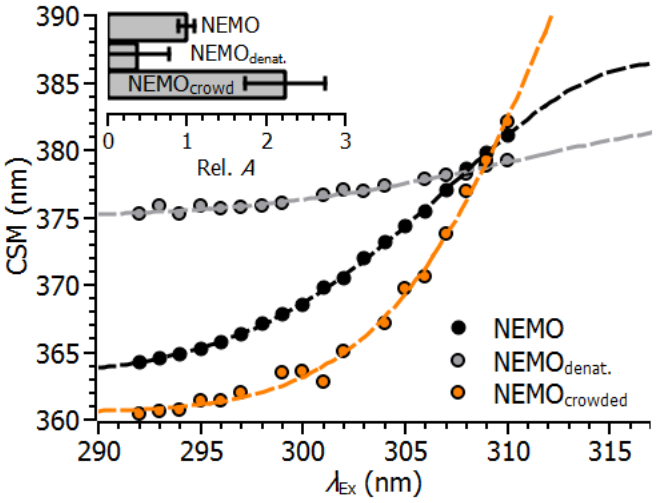
NEMO
NEMOdenat.
NEMOcrowd
0
1
2
3
Rel. A
390
385
380
375
370
365
360
CSM (nm)
290
295
300
305
310
315
λEx (nm)
NEMO
NEMOdenat.
NEMOcrowded

Figure 5.

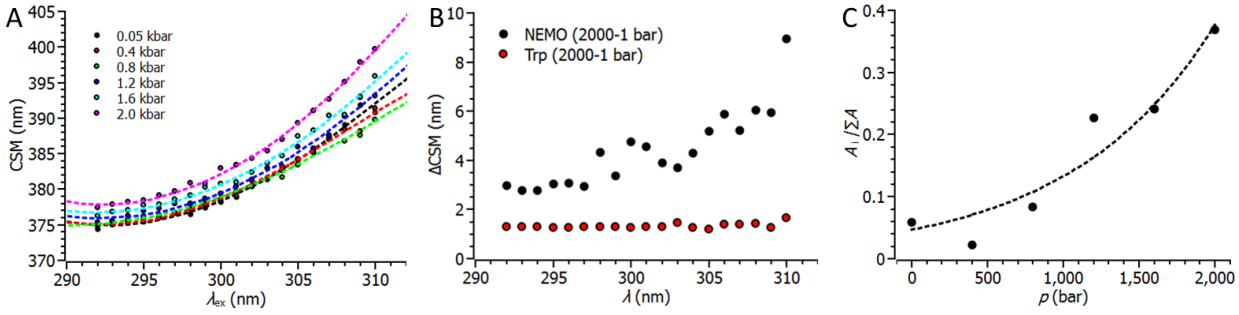
A
B
C
0.05 kbar
0.4 kbar
0.8 kbar
1.2 kbar
1.6 kbar
2.0 kbar
CSM (nm)
λex (nm)
NEMO (2000-1 bar)
Trp (2000-1 bar)
ΔCSM (nm)
λ (nm)
A1 /ΣA
p (bar)

Figure 6.

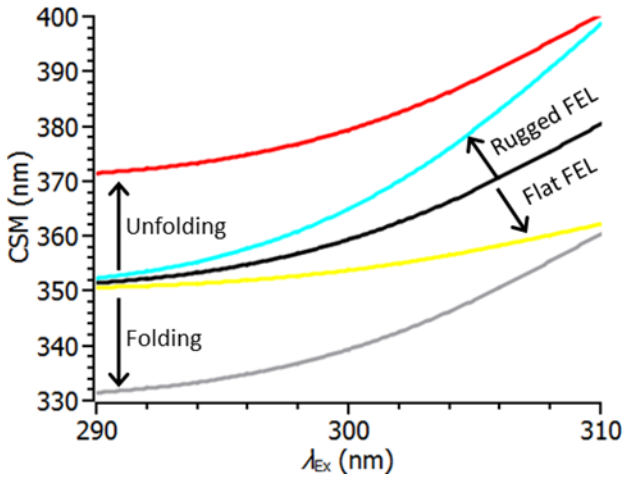
400
390
380
370
360
350
340
330
CSM (nm)
Unfolding
Folding
Rugged FEL
Flat FEL
290
300
310
λEx (nm)

Figure 7.

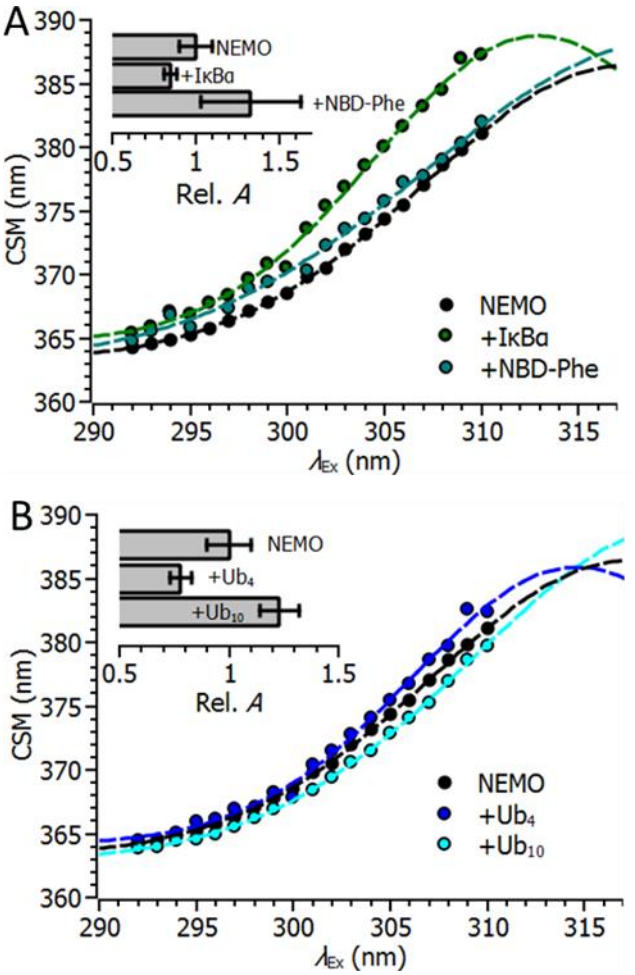

Figure 8.

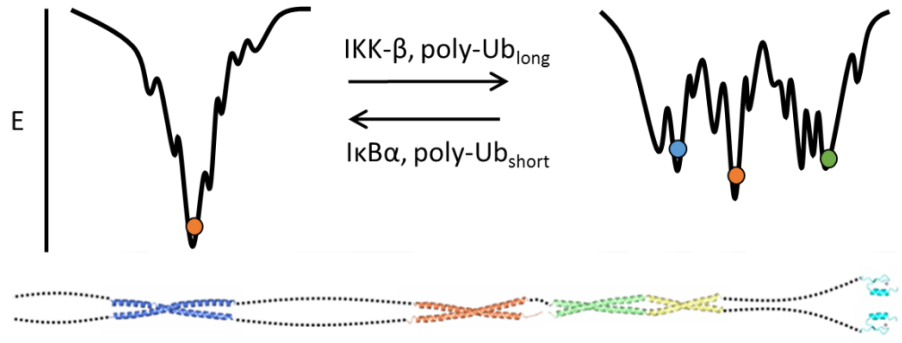

Figure 9.